Journal of Materials Chemistry C

Accepted Manuscript

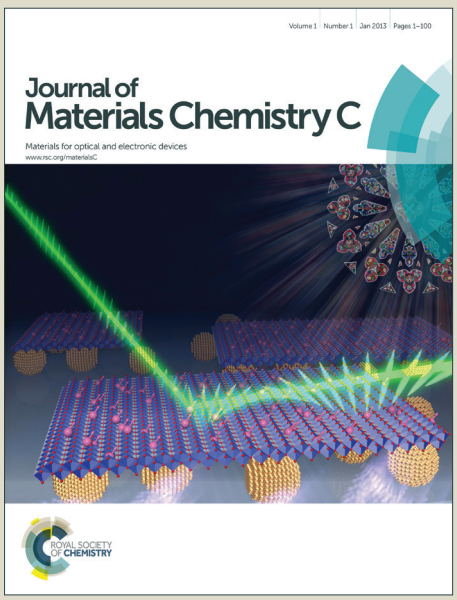

ROYAL SOCIETY OF CHEMISTRY

www.rsc.org/materialsC

Cite this: DOI: 10.1039/c0xx00000x

www.rsc.org/xxxxxx

ARTICLE TYPE

Chemically Deposited PbS Thin Film Photo-Conducting Layers for Optically Addressed Spatial Light Modulators

Tsofnat Safrani[1,3], Tatipamula Arun Kumar[2,3], Matvey Klebanov[2,3], Neta Arad-Vosk[4], Rotem Beach[4], Amir Sa'ar[4], Ibrahim Abdulhalim[2,3], Gabby Sarusi[2,3] and Yuval Golan[1,3]

Received (in XXX, XXX) Xth XXXXXXXXX 20XX, Accepted Xth XXXXXXXXX 20XX
DOI: 10.1039/b000000x

Abstract

Lead sulfide semiconducting thin films were chemically deposited on indium tin oxide coated glass plates for use as photoreceptor layers in conjugation with optically addressed spatial light modulators (OASLMs). Deposition conditions such as temperature, reagent concentration, pH and deposition time were optimized in order to achieve homogeneous, continuous and adherent films. Mirror-like films with tunable particle size and film thickness were obtained. The microstructure and morphology evolution of the films were investigated using X-ray diffraction, scanning electron microscopy and atomic force microscopy. Electrical and optical properties were studied using four-point probe measurements, FTIR spectroscopy, photoluminescence spectroscopy, photo-current and photo-voltage measurements. Blue shift of the band gap to the short wavelength infra-red (SWIR) range was obtained as a function of particle size, and significant photovoltaic effect was measured. The resistivity of the films, as well as their photo-voltage response, were enhanced after thermal annealing. These results indicate that PbS films can serve as effective photoreceptors in OASLMs for applications including SWIR detection for night vision purposes.

1. Introduction

Lead chalcogenides are technologically important semiconducting materials with infra-red (IR) sensitivity, suitable for use as IR detectors, IR emitters, solar control coatings and other optical applications.[1-3] PbS as well as other narrow band gap semiconductors (Ge, InSb, InGaAs, HgCdTe) is commonly used for these purposes. There are several techniques for fabricating high quality PbS thin films, where chemical bath deposition is one of the simplest and cost effective methods. Chemically deposited PbS thin films can be easily integrated on almost any substrate and its band gap energy can be tuned from 0.41eV (3μm) of the bulk material to shorter wavelengths, down to the short wavelength infra-red (SWIR) range (1.55μm, 0.8eV) depending on grain size due to the quantum confinment effect.[4-6] PbS is a good alternative to other narrow band gap semiconductors for integration in electric and opto-electric devices due to its relatively large Bohr radius of 18nm so that quantum confinment effects can take place at relatively large grain size. Optically addressed spatial light modulators (OASLMs) have emerged in the last two decades as essential components for optical processing and manipulation.[7] The general configuration of an OASLM device is comprised of two components: the photoreceptor and the electro-optic material. These layers are often separated by a dielectric mirror and sandwiched between two indium tin oxide (ITO) electrodes.[8] Irradiation activates the photoreceptor which produces a corresponding charge field on the electro-optic material. Semiconducting materials such as cadmium sulfide[7, 9] amorphous silicon[10], or gallium arsenide[10, 11] are commonly used as photoreceptors, and the most commonly used electro-optic materials are nematic liquid crystals (LC), either in the parallel or twisted configuration[12]. Applications can be found in a wide range of wavelengths from visible to the near IR (< 1.1μm).[11] *Wang et al.* have developed an IR-OASLM with $In_{0.53}Ga_{0.47}As$-InP photosensor sensitive to 1.55 μm write light (SWIR range).[11] Sensing in the SWIR is very attractive for applications such as passive night vision, biomedical imaging and remote sensing.[4] For passive night vision, SWIR detection is of great interest because of three major advantages: there is a strong moon and cloud glow in this range, and because of the relatively short IR wavelength the resolution is better and there is no need for cooling. However, no studies have focused on IR photosensors in OASLMs, nor on PbS thin films chemically deposited directly on ITO substrates for OASLMs. OASLMs have major adventages over electronically addressed spatial light modulators since they do not require complicated electronic components, pixels, special driving schemes and cooling instruments. Thus, the device can be

transparent, low in weight and size, while providing high resolution imaging. In this work, we have studied the morphology evolution, structure, electrical and optical properties of PbS thin films chemically deposited on ITO coated glass plates. The goal was to optimize the deposition conditions in order to achieve homogeneous, continuous and adherent films with tunable particle size and thickness to serve as photoreceptor for OASLM based applications. Ultimately, the main goal was to reach a high quality PbS film with photovoltaic effect in the SWIR range that can be used for passive night vision applications. The deposition parameters such as temperature, reagent concentration, pH and deposition time were optimized and eventually single phase, homogenous, continuous and adherent, mirror-like films with tuable particle size and thickness were obtained. The electrical and optical properties such as sheet resistance, photo-current, photo-voltage, optical absorption, and photoluminescence were investigated. Blue shift of the band gap towards the SWIR range was obtained in films with nanometer size grains. Relatively high absorbance and resistance were measured and significant photo-response, that was enhanced after anealing, was detected.

2. Experimental section

2.1 Materials and Chemicals

PbS thin films were deposited from solutions containing $Pb(NO_3)_2$, $CS(NH_2)_2$ and NaOH under various experimental conditions. Lead nitrate (Aldrich, analytical 99.99+%), thiourea (TU) (Aldrich, ACS ≥99.0%) and sodium hydroxide (Gadot, AR) were used without further purification. ITO coated glass plates (1.5×1.7 cm^2 rectangles), cleaned by wiping with ethanol, were used for substrates. For the photo-current and photo-voltage measurements films were deposited directly on the glass plates. Distilled water was obtained using a Millipore Direct Q3 and ~10% HCl solution (Gadot, AR) was used for etching.

2.2 Chemical Bath Deposition

Films were deposited according to the procedure described in previous works, which was optimized for the growth of PbS films on GaAs[13] or on Si[14] substrates. This procedure was modified and optimized for growth on ITO coated glass plates and the final composition of the deposition solution was: 44 mM NaOH, 9 mM $Pb(NO_3)_2$, and 20.5 mM $CS(NH_2)_2$, mixed in this order. Under these deposition conditions a turbid solution is obtained upon addition of the Pb precursor due to reaction of the lead cations with hydroxide anions to form a suspension of insoluble lead hydroxide ($Pb(OH)_2$). Prior to deposition, the solution contained in a Pyrex beaker was purged with pure N_2 for 60 min in order to minimize levels of dissolved oxygen and carbon dioxide, and placed in the dark in a thermostatic bath for thermal equilibrium. As the desired deposition temperature was reached, the last reactant was added. The growth of PbS films was carried out under various deposition time and temperatures and at different reagent concentrations. Films were deposited on the bottom face of the substrates in order to prevent large particles from adhering to the growing film. Therefore, the substrates were placed with the ITO face down in the solution, mounted on a custom-designed Teflon stage at an angle of ~70° with respect to the surface. During deposition, the upper face of the substrate (which is the bare glass face) is covered with a thick PbS layer formed by sedimentation rather than by adsorption. This layer was removed by wiping with ~10% HCl solution, and the samples were rinsed with ethanol following by drying with a stream of ultrapure (99.999%) N_2 gas. Films were investigated before and after air annealing at 100°C-200°C for 1h-2h.

2.3 Characterization Methods

2.3.1 X-Ray Diffraction (XRD)

Diffraction data were collected on a Panalytical Empyrean powder X-Ray diffractometer equipped with a position sensitive X'Celerator detector using Cu K_α radiation (λ=1.5405 Å) operating at 40 kV and 30 mA. The Bragg-Brentano geometry was employed. θ/2θ scans were run during 10 min in a 2θ range of 20-65° with step size of 0.0334° and 0.445 sec per step.

2.3.2 High Resolution Scanning Electron Microscopy (HR-SEM)

The morphology of the films was observed using a JEOL 7400F field emission gun SEM without coating the samples. Secondary electrons were used to obtain the images in all cases. Acceleration voltage of 3.5 kV and a current of 10 mA were used.

2.3.3 Atomic Force Microscopy (AFM)

Samples were gently scratched with sharp tweezers. The height of the scratch was measured using a Dimension 3100 (Veeco) AFM. The instrument is mounted on an active anti-vibration table and operated in tapping mode using a 100 μm scanner. Section analysis were performed and typically ranged over 30μm scan at a scan rate of 1 Hz.

2.3.4 Electrical and Optical Properties

2.3.4.1 Four-point probe measurements (FPP)

Sheet resistance was measured by applying the four-point probe technique using a Jandel RM3000 unit, equipped with a linear array tungsten carbide four-point probe head.

2.3.4.2 SWIR-NIR Spectroscopy

Transmission measurements were performed using a Bruker Vertex V70 FTIR, equipped with deuterated triglycine sulfate (DTGS) detector. Measurement range: 600-8000 cm^{-1}. Reflection was measured with a Cary 5000 UV-VIS-NIR spectrophotometer at a wavelength range of 400-3000 nm and the absorbance was calculated according to A=1-R-T. The absorption coefficient α, was taken as -log(T) divided by the film thickness (in cm), where T is the transmission of the PbS film which is obtained after dividing the sample curve (of PbS film on ITO coated glass) by the substrate curve (the ITO coated glass). Band gap energy was calculated by plotting $(\alpha h\nu)^2$ as a function of the excitation energy, $h\nu$, where the intersect of the extrapolated straight line with the x axis is E_g.

2.3.4.3 Photoluminescence (PL)

Ar^+ laser (488 nm) was used as excitation source with power density of about 15W/cm^2 for a spot of 2mm^2. The signal was measured by a mercury cadmium telluride (MCT) photovoltaic detector and analyzed by a Bruker Vertex V70 FTIR. Noise and thermal effects were reduced using a lock-in-amplifier.

2.3.4.4 Photo-current (PC) and Photo-voltage (PV)

A Keithley Instruments model 610C electrometer was used for PC and PV measurements. Halogen lamp, coupled with two filters for the SWIR range, was used for illumination. A 1400-1700 nm wavelength filter with power density of about 1000 μW/cm^2 and 1550 nm wavelength filter with power density of about 337 μW/cm^2. Samples were prepared by evaporating two 0.3cm×1.5cm indium contacts on the 1.7 cm×1.5 cm PbS film,

thus forming 1.1cm×1.5cm bare PbS film.

3. Results and Discussion

This work was focused on optimization of the chemical deposition process for growing PbS semiconducting thin films on ITO coated glass plates for optical applications. For this purpose, the influence of deposition parameters such as time, temperature and reagent concentrations on the morphology and physical properties of the films were examined. Annealing effects were also investigated. XRD, SEM and AFM were applied for morphological and structural characterization. Electrical and optical properties were examined using PL, FPP, PC, PV and transsmision measurements.

3.1 Morphology evolution and optimization

Film morphology was investigated as a function of NaOH concentration that defines the solution pH. Fig. 1a and 1b shows XRD spectra and SEM images, respectively, of films deposited from solutions containing variable concentrations of NaOH. Fig. 1c shows (200)/(111) intensity ratio (red) and sum of the total (200) and (111) peak area (green) that is correlated to film thickness (correlated to the amount of crystalline diffracting material).

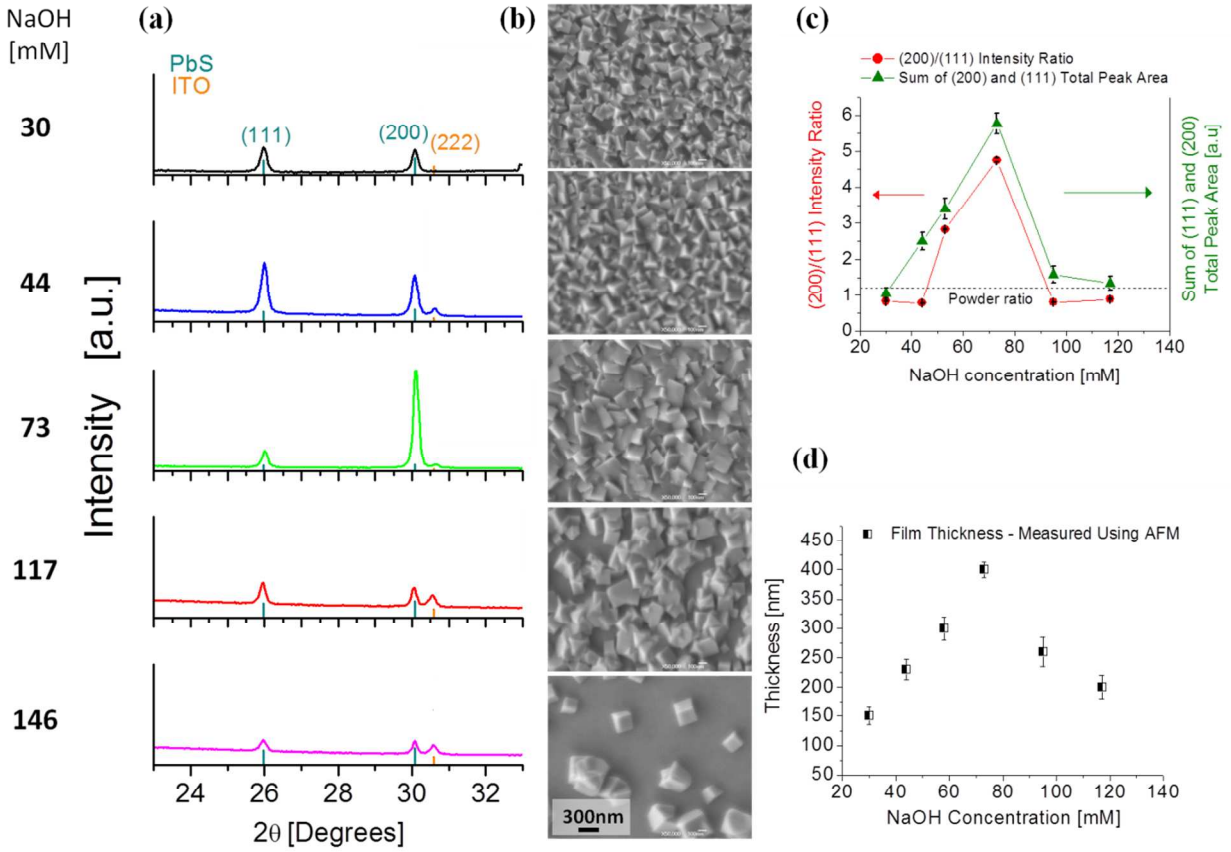

Figure 1: The effect of NaOH concentration: (a,b) XRD patterns and SEM images of films deposited with different NaOH concentrations. (c) (200)/(111) peak intensity ratio (red) and total peak area (green). (d) Film thickness measured using AFM.

Fig. 1d shows the thickness (measured by AFM) vs. NaOH concentration. These films were deposited from solution containing 20.5 mM TU and 9 mM $Pb(NO_3)_2$. A typical dependence of thickness on pH was observed; the film thickness increasing with pH up to a maximum value and then decreasing. This behavior is a result of two competing processes that are controlled by the OH^- ions concentration; the first is release of S^{2-} ions from pH dependent decomposition of TU which accelerates growth rate. The second is the complexation of free Pb^{2+} ions by hydroxide anions, which decelerates growth rate.[15] Maximum growth rate/thickness was obtained with 73 mM NaOH. Deposition with lower NaOH concentrations occurs under sulfide-limited conditions. In this case increasing NaOH concentration results in a higher concentration of free sulfide ions that accelerates growth rate. Deposition at NaOH concentrations > 73 mM occurs under lead limited conditions. In this case increasing NaOH concentration results in a lower concentration of free lead cations which decelerates growth rate. Thus, the deposition at concentrations < 73 mM resulted in films with lower thicknesses and smaller particles, while the deposition at C > 73 mM resulted in discontinuous films or randomly distributed particles. There is a good correlation between the total peak area (green curve in Fig. 1c) and the thickness vs. NaOH concentration curve (Fig.1d). Interestingly, films texture (red

curve in Fig. 1c) is in good agreement with both. A (200) preferred orientation was obtained with 73 mM NaOH. This preferred orientation was eliminated as the thickness of the films decreased. Such behavior was demonstrated before as film texture tends to develop with film thickness (or deposition time). *Osherov et al.* reported similar behavior in PbS films deposited on GaAs substrate.[13] This behavior originates from changes in the deposition growth mechanisms; namely, transitions from cluster growth mechanism to ion-by-ion growth mechanism which occur due to changes in reagent concentrations.[13,15] According to the results shown in Fig. 1, the optimal NaOH concentration was determined to be 44 mM in which a relatively slow and controlled deposition process occurs. Under these conditions, continuous, and adherent films were obtained.

Film morphology was also investigated as a function of TU concentration (at constant NaOH concentration of 44 mM).

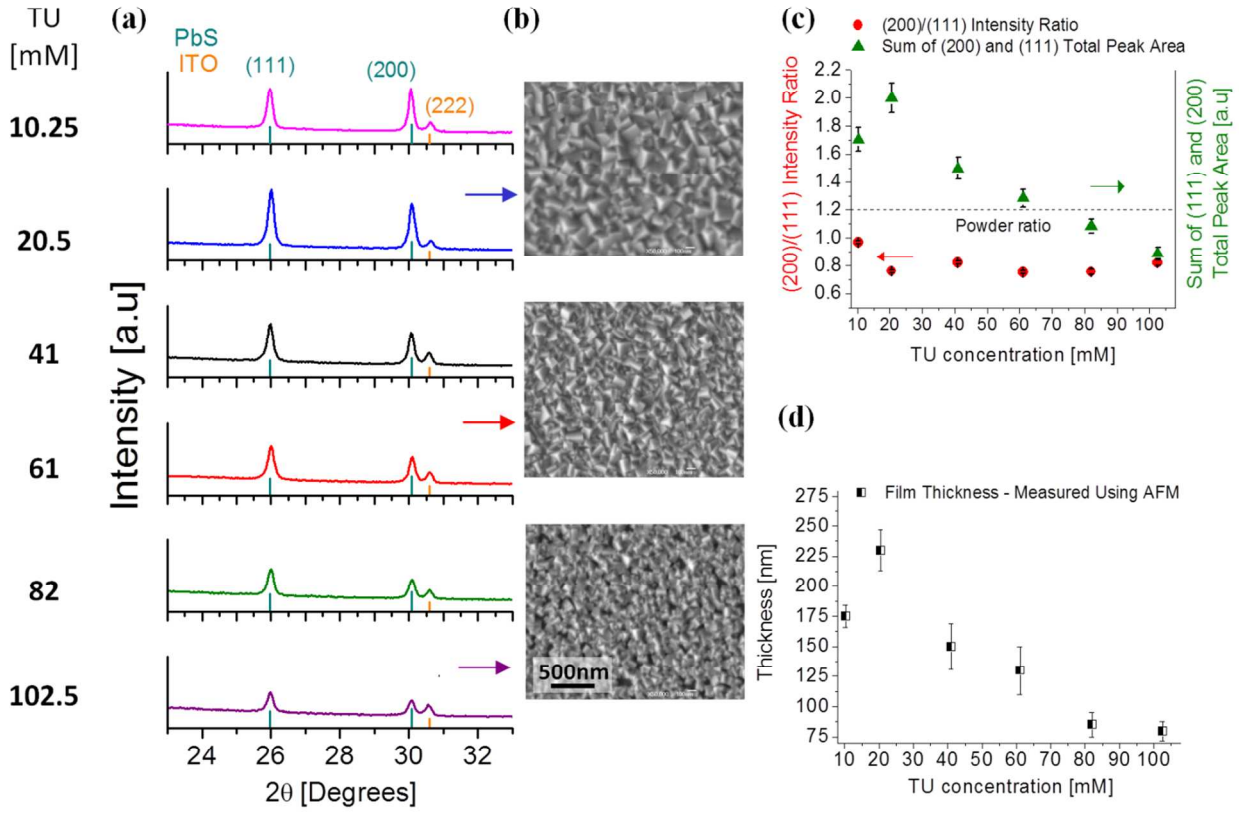

Figure 2: The effect of TU concentration: (a,b) XRD patterns and representative SEM images for films deposited with different TU concentrations. (c) (200)/(111) peak intensity ratio (red) and the total peak area (green). (d) Film thickness measured using AFM.

Fig. 2a and 2b shows XRD spectra and SEM images, respectively, of films deposited from solutions containing variable TU concentrations. Fig. 2c shows (200)/(111) intensity ratio (red) and sum of the total (200) and (111) peak area (green). Fig. 2d shows film thickness as measured using AFM vs. TU concentration. As aforesaid, the deposition occurs under sulfide-limited conditions, where increased TU concentration affects the concentration of OH^- ions that is consumed for TU decomposition and subsequent release of free S^{2-} ions. This accelerates growth rate as can be seen at the first two points in Fig. 2d. However, excess of TU will rapidly consume the OH^- ions, creating many small nucleii that do not develop under the reduced pH conditions. This eventually results in reduced growth rate and as a result, very thin, discontinuous films were obtained. Also here, a good correlation was obtained between the total peak area (green curve in Fig. 2c) and the thickness vs. TU concentration (Fig. 2d). The red curve in Fig. 2c shows almost no effect of the TU concentration on film texture; there is a slight tendency towards (111) texture that do not change much with increasing TU concentration.

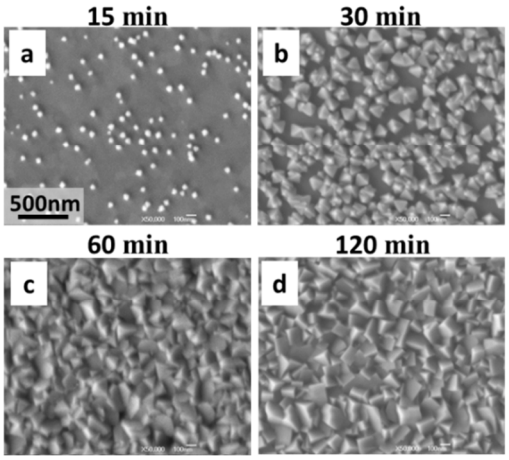

Figure 3: HR-SEM images of PbS particles/films deposited on ITO coated glass substrates at 30 ºC for different periods of time.

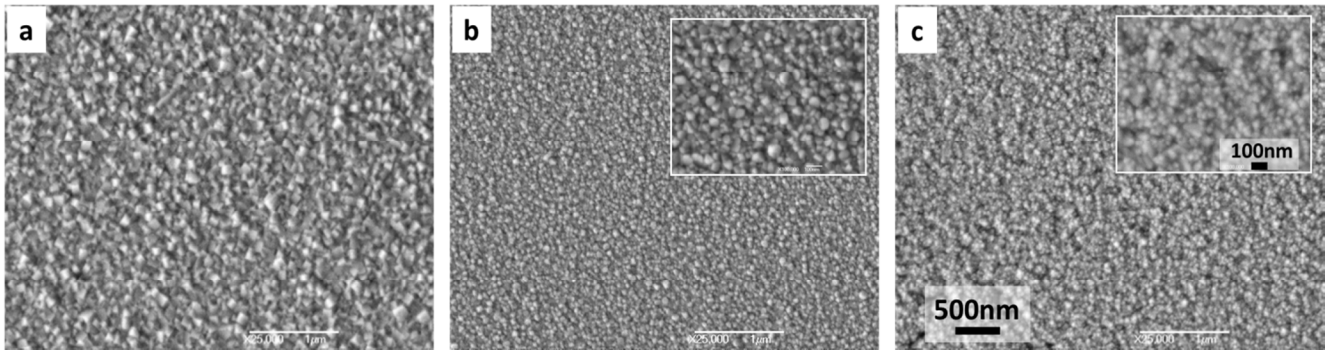

Figure 4: HR-SEM images of PbS films deposited on ITO coated glass substrates for (a) 24 h at 10 ºC, (b) 24 h at 0 ºC and (c) 10 h at 0 ºC followed by another 10 h at 0 ºC. The insets show higher magnifications.

According to these results, the optimal TU concentration was determined to be 20.5 mM in which continuous films with sufficient thickness were obtained. In all of the above cases, films were deposited under standard conditions of 30 ºC for 120 min. Under these conditions, 'bulk' particles larger than 100 nm (hence, above the critical dimensions threshold for quantum size effects) were obtained.In order to reach nm size (size quantized) particles, optimization of deposition time and temperature was required. Film evolution with time (Fig. 3) indicated isolated nanoparticles (Fig. 3a) or discontinuous films (Fig. 3b) at the early stages of deposition. Only after 120 min of deposition, continuous films start to develop.

3.2 Tunability of particle size and energy band gap

Deposition at lower temperatures resulted in films with much smaller particles (Fig. 4). At 10 °C, 50-70 nm particles were obtained (Fig. 4a) and at 0 °C, ca. 20 nm particles were obtained (Fig. 4b). In both cases, the thickness of the films was ~100 nm as measured in AFM. Deposition was possible down to a low temperature limit of -2 ºC (solution freezing point). Thus, further decrease in particle size was achieved by shorter deposition time. Low deposition temperature together with shorter deposition time resulted in much smaller particles composing very thin films, almost discontinuous. Since continuity and thickness are important for higher absorption and photo-effects, successive deposition process was conducted. In this case, films with particles lower than 10 nm in diameter were obtained (Fig. 4c). XRD patterns of single-phase polycrystalline PbS films (JCPDS powder diffraction file 5-592) deposited on ITO coated glass are shown in Fig. 5. The inset compares the broadening of (111) Bragg peak for four different samples deposited at different temperatures. The low signal to noise ratio in the purple and orange spectra are due to the very small thickness of the films. Full width half-maximum values were extracted in order to calculate the crystal coherence length using the *Scherrer* formula (Eq. 1), where λ is the wavelength, β is the peak broadening (in Radians), θ is the Bragg angle and K is a geometrical factor (for round shaped crystals $K = 1$).

$$D = \frac{K\lambda}{\beta \cos\theta} \qquad (1)$$

Lower deposition temperatures resulted in broader XRD peaks, indicating smaller grain size. Correspondingly, PL measurements showed blue shift of the band gap energy with decreasing particle size (Fig. 6) as expected from the particle in a box model. Lower deposition temperatures together with shorter deposition times resulted in a strong blue shift of the band gap towards the SWIR range up to 0.72 eV.

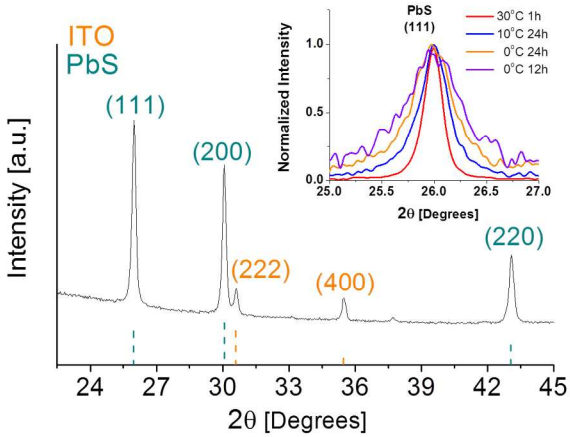

Figure 5. XRD pattern of PbS film on ITO coated glass substrate. The inset shows (111) peak of three samples deposited at different temperatures for various periods of time.

The band edge, E_g, as a function of the particle size was calculated according to the simple effective-mass approximation model that predicts the effective band gap energy due to three-dimensional confinement with respect to the bulk value (Eq. 2).[16] Where E_g is the band gap of the bulk semiconductor, r is the radius of the particle, m^*_e is the electron effective mass, m^*_h is the hole effective mass, ε is the dielectric constant of the semiconductor and e is the electric charge.

$$E_g^{'} = E_g + \frac{\hbar^2\pi^2}{2r^2}\left[\frac{1}{m_e^*}+\frac{1}{m_h^*}\right] - \frac{1.786e^2}{\varepsilon r} - \frac{0.124e^4}{\hbar^2\varepsilon^2}\left[\frac{1}{m_e^*}+\frac{1}{m_h^*}\right]^{-1} \quad (2)$$

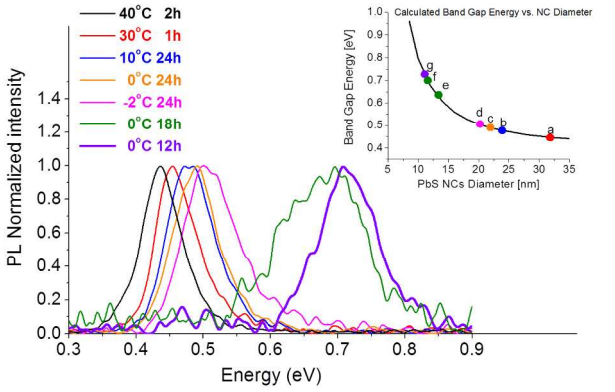

Figure 6. Photoluminescence spectra obtained from films deposited at different temperatures for different periods of time: 40 °C for 2h, 30 °C for 1h, 10 °C for 24h, 0 °C for 24h, -2 °C for 24h, 0 °C for 18h and 0 °C for 12h. The inset shows the calculated band gap energy curve vs. crystallite diameter, were the denoted points ***a, b, c, d, e-f,*** and ***g*** correspond to the measured band-to-band PL energy of the different films. Table 1 compares the particle size values calculated from XRD and PL.

Table 1. Crystal size calculated from XRD (Scherrer line broadening) and PL.

Sample	Crystal size (in Diameter) based on:	
	XRD	PL
30°C 1h	64 nm ± 3 nm	32 nm ± 3 nm
10°C 24h	29 nm ± 2 nm	24 nm ± 6 nm
0°C 24h	20 nm ± 2 nm	22 nm ± 6 nm
-2°C 24h	17 nm ± 3 nm	20 nm ± 2 nm
0°C 12h	15 nm ± 3 nm	11 nm ± 2 nm

Similar crystal size values were obtained at low temperature deposited films, however, for films deposited at higher temperatures, the XRD and PL showed quite different values. This may be related to the wider particle size distribution and different geometry; films deposited at low temperature were composed of small spherical particles with narrow size distribution, while films deposited at higher temperatures comprised of cubical particles with wider size distribution. These are likely to present errors in the grain size estimation from both XRD and PL methods.

3.3 Electrical and Optical properties

As mentioned earlier, the commonly used electro-optic material in OASLMs are nematic liquid crystals that react in response to voltage change. Thus, it is required that the photoreceptor layer will generate a significant photo-voltage response. Additional properties required are relatively high absorbance for higher efficiency and relatively high dark resistance for high voltage change on the liquid crystals. PbS is a semiconducting material and thus it is partially conductive. However, films composed of nanometer-sized particles will be much more resistive because of the profusion of grain boundaries. Moreover, mild thermal treatment such as annealing in air can increase film resistance due to particle surface oxidation. FPP measurements indicated a significant increase in film resistance for the nanometer-sized particle films, in comparison with film composed of larger particles. A major increase of two orders of magnitude was detected (Table 2). Annealing of these samples resulted in additional increase of one order of magnitude in sheet resistance (Table 2). We assume that annealing in air environment creates an ultrathin oxide layer on the particle surface; XRD peak broadening together with a slight decrease in peak intensity after annealing (not shown here) support this assumption.

Table 2. Sheet resistance of films deposited at different temperatures before and after annealing, as measured by FPP method.

Sample	Sheet resistance [MΩ]	
	Before Annealing	After Annealing
30°C 1h	0.024	0.2
0°C 24h	3	20
-2°C 24h	12	140

Transmission measurements showed relatively high absorbance; up to 50 percent in the SWIR region for bulk sample (see Fig. 7a). The bends in the absorption spectra (especially in the black curve corresponding to bulk PbS) originate from interference effects. Reflectance was found to range between 30% in the visible and 20% in the SWIR. Reflectance in the SWIR can be overcome with anti-reflecting coating and the relatively high reflectance in the visible is an advantage, if the OASLM device is designed to operate in a reflective mode (which is the case in many applications). Films comprised of nm-size particles deposited at lower temperatures showed lower absorbance due to their lower thicknesses. Fig. 7b shows the absorption coefficient α as a function of hv. This way the relative absorbance can be normalised with respect to the different thicknesses of the films. Direct band gap energy values were calculated from the plot of $(\alpha hv)^2$ as a function of the energy, hv, where the intersect of the extrapolated straight line with the x axis provides an estimation of E_g (Fig. 7c).

Table 3. Band gap energy and absorption coefficient based on absorption and PL

Sample	Band gap energy based on:		α [1/cm] × 10^4 at 0.9 eV
	PL (±0.04eV)	Absorption (±0.05eV)	
40°C 2h	0.43	0.41	4
30°C 1h	0.45	0.46	3
10°C24h	0.47	0.47	9
0°C 24h	0.49	NA	NA
-2°C 24h	0.51	0.53	12
0°C 12h	0.72	0.76	13

Notably, there is an increase in the absorption coeficient values with decreasing particle size in the SWIR range. Absorption coefficient values at 0.9 eV were extracted from the data and are summarized in Table 3 (interference effects were taken into account). Direct band gap energy values were found to be: 0.41 eV for the bulk sample and for smaller particle films 0.46, 0.47, 0.53 and 0.76 eV were obtained. These values are in good correlation with those measured by PL (see Table 3).

Cite this: DOI: 10.1039/c0xx00000x

www.rsc.org/xxxxxx

ARTICLE TYPE

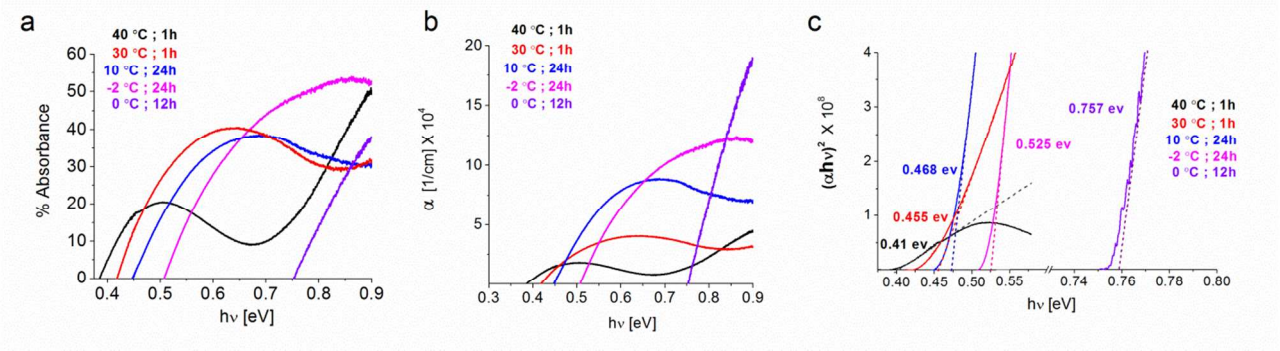

Figure 7: (a) Absorbance vs. energy (b) absorption coefficient α vs. energy (c) plot of $(\alpha h\nu)^2$ as a function of the energy, $h\nu$, for films deposited at different temperatures.

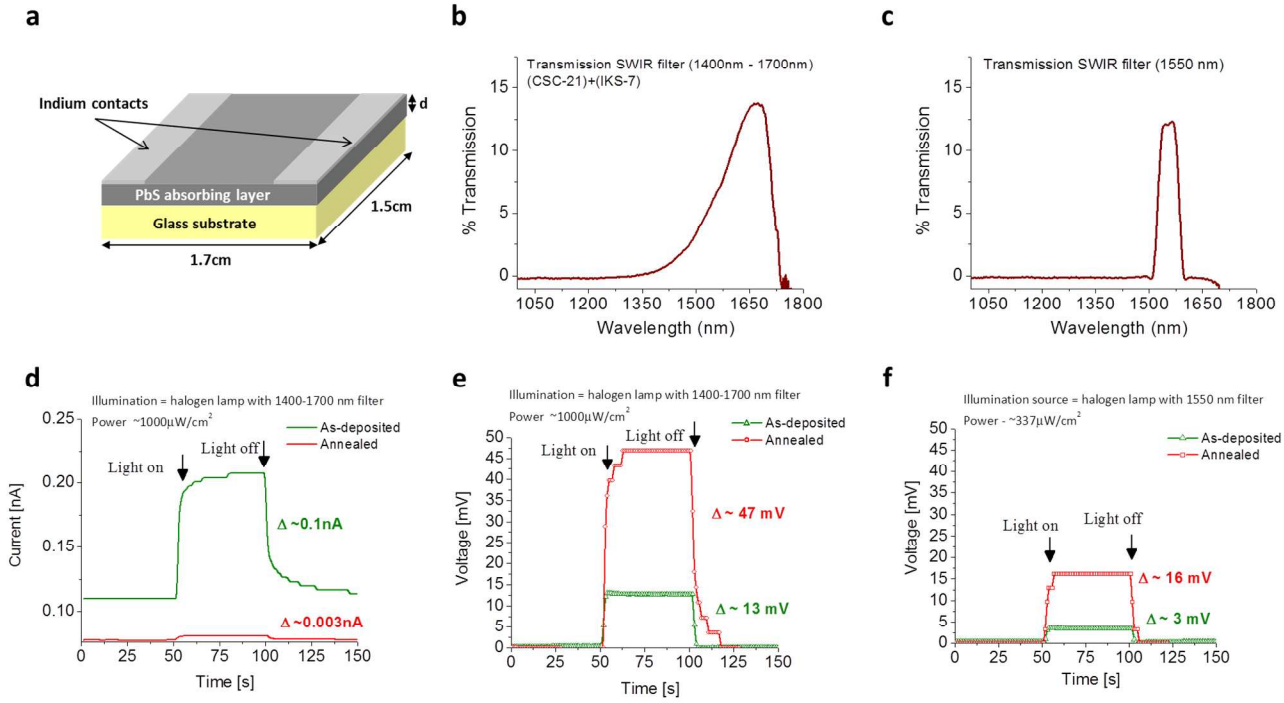

Figure 8. (a) Sample set up for photo-current and photo-voltage measurements (b) Optical transmission spectrum using a 1400-1700 nm wavelength filter (c) Optical transmission spectrum using a 1550 nm wavelength filter (d) Photo-current rise and decay curve under 1400-1700 nm illumination (e) Photo-voltage rise and decay curve under 1400-1700 nm illumination and (f) Photo-voltage rise and decay curve under 1550 nm illumination. Measurements were performed on as-deposited and annealed PbS film with $E_g = 0.71$ eV.

Some of the values differ from each other within the error range; however, the trend is distinct. Photo-voltage measurements revealed significant photovoltaic effect (see Fig. 8). These measurements were obtained from nanoparticle PbS thin film with 0.71 eV E_g (deposited at 0 °C for 10 h followed by another 10 h of deposition). However, all samples showed similar results in which the photovoltaic effect was significantly intensified after annealing. Figures 8a, 8b and 8c shows the sample setup, the spectrum of 1400-1700 nm wavelength filter and the spectrum of 1550 nm wavelength filter, respectively. Fig. 8d shows the rise and decay curve of the photo-current under halogen lamp illumination with 1400-1700 nm filter and 1V external voltage. As deposited film showed dark current of 0.11 nA, and considering bias voltage of 1V, the resistance is almost 10 GΩ. The measured light current was almost two times higher (0.2 nA). After annealing, the dark current decreased to 0.077 nA and the current change upon illumination was also smaller, only 4% change. This is due to the higher resistance of the annealed film. Fig. 8e shows the photo-voltage rise and decay curve under the same illumination, and revealed significant photo-voltage

response of about 13 mV change for the as-deposited film and 47 mV change for the annealed film. Fig. 8f shows the photo-voltage rise and decay curve under 1550 nm illumination, in which a response of about 3 mV change was obtained for the as-deposited film and 16 mV for the annealed film. It is not clear yet what is the mechanism in which the photo-injected charge is activated, and further studies will be carried out to address this issue. One of the possibilities is the photo-Dember effect[17] that is very common in semiconducting materials. In bulk PbS, the photo-Dember effect is unlikely since the mobility of electrons and holes is similar, however, very small diversions from symmetry or polarity may initiate the photo-Dember effect. Small changes in the film thickness along the plane, non-uniform light illumination (the illumination spot size was 4mm in diameter projected onto a 11mm X 15mm PbS thin film) and surface oxidation of the films or the single nano-particles; all these are possible factors that can be resposible for the high photovoltaic effect that was detected. Additionally, in the case of nanoparticles with possibly oxidized surface, especially after annealing in air, differences in actual mobilities may arise.[18] This photo-injected charge phenomena was observed in several different samples of nanoparticle films and increased with the decrease in particle size (with the increase in E_g). It was significant and repeatedly enhanced after annealing in all samples. This suggests that PbS nanoparticle films can create sufficient photo-voltage response for the operation of an OASLM in the SWIR range.

4. Conclusions

Uniform, single phase, mirror like nanostructured PbS thin films with tunable band-gap energies were successfully deposited on ITO coated glass plates. The morphology and properties of these films are strongly affected by the deposition parameters and can be controlled by altering the solution pH, temperature, time and reagent concentrations. Relatively low deposition temperatures together with short deposition time resulted in a strong blue shift of the energy band gap. Relatively high absorbance together with high resistance and photovoltaic effect indicate that these films are potentially suitable for use as photoreceptors in optically addressed spatial light modulators. Tuning the PbS photoreceptor energy band gap up to the SWIR range can allow utilization of these photo-absorbing films for night vision applications active in the SWIR.

Notes and references

[1] Department of Materials Engineering, Ben-Gurion University of the Negev, Beer-Sheva 84105, Israel.
[2] Department of ElectroOptics Engineering, Ben-Gurion University of the Negev, Beer-Sheva 84105, Israel.
[3] Ilse Katz Institute for Nanoscale Science and Technology, Ben-Gurion University of the Negev, Beer-Sheva 84105, Israel.
[4] Racah Institute of Physics and the Harvey M. Kruger Family Center for Nanoscience and Nanotechnology, the Hebrew University of Jerusalem, Jerusalem 91904, Israel.
Fax: +972-8-6472944; Tel: +972-8-6466297; E-mail: ygolan@bgu.ac.il

Acknowledgements

We thank Dr. Avner Safrani, Dr. Dmitry Mogilyansky and Roxana Golan for expert assistance in photocurrent measurements, XRD and AFM, respectively. This work was partially funded by the focal technological areas (FTA) program of the Israeli National Nanotechnology Initiative (INNI), and was partially funded by the Israel Science Foundation, Grant #156/14.

References

1. Nair, P. K.; Nair, M. T. S.; Fernandez, A.; Ocampo, M., Prospects of chemically deposited metal chalcogenide thin films for solar control applications. *J. Phys. D: Appl. Phys.* **1989,** 22, 829-836.
2. P. Capper; C.T. Eliot, *Infrared Detectors and Emitters: Materials and Devices*. Kluver Academic Publishers: 2001.
3. Nair, P. K.; Nair, M. T. S., PbS solar control coatings: safety, cost and optimisation. *J. Phys. D: Appl. Phys.* **1990,** 23, 150-155.
4. Vavilov, V. P.; Hansen, M. P.; Malchow, D. S.; Burleigh, D. D., Overview of SWIR detectors, cameras, and applications. **2008,** 6939, 69390I-69390I-11.
5. Heves, E.; Gurbuz, Y., PbS Colloidal Quantum Dot Photodiodes for SWIR Detection. *Procedia Engineering* **2012,** 47, (0), 1426-1429.
6. Osherov, A.; Makai, J. P.; Balazs, J.; Horvath, Z. J.; Gutman, N.; Sa'ar, A.; Golan, Y., Tunability of the optical band edge in thin PbS films chemically deposited on GaAs(100). *J Phys Condens Matter* **2010,** 22, (26), 262002.
7. Efron, U.; Liverscu, G., *Spatial Light Modulator Technology: Materials, Devices and Applications*. Marcel Dekker: 1995.
8. Mirhaj, M. H.; Dizaji, H. R.; Ehsani, M. H.; Siyanaki, F. H., Substrate Temperature Effect on Physical Properties of In-doped CdS Thin Film. *Chalcogenide Letters* **2012,** 9, (5), 193-199.
9. Lu, K.; Saleh, B. E. A., Complex amplitude reflectance of the liquid crystal light valve. *Applied Optics* **1991,** 30, 2354-2362.
10. Armitage, D.; Thackara, J. I.; Eades, W. D., Photoaddressed liquid crystal spatial light modulators. *Appl. Opt.* **1989,** 28, 4763–4771.
11. Wang, L.; Moddel, G.; Burdge, G. In *Design of an Optically Addressed Spatial Light Modulator Sensitive to 1.55μm Write Light*, Spatial Light Modulators and Applications, Salt Lake City, Utah, March 14-16, 1995; Salt Lake City, Utah, 1995.
12. Efron, U.; Wu, S. T.; Bates, T. D., Nematic liquid crystals for spatial light modulators: recent studies. *Journal of the Optical Society of America B* **1986,** 3, (2), 247-252.
13. Osherov, A.; Ezersky, V.; Golan, Y., Microstructure and morphology evolution in chemically deposited semiconductor films: 4. From isolated nanoparticles to monocrystalline PbS thin films on GaAs(100) substrates. *Eur. Phys. J. Appl. Phys.* **2006,** 37, (1), 39-47.
14. Osherov, A.; Golan, Y., Chemical solution deposited PbS thin films on Si(100). *Phys. Status Solidi C* **2008,** 5, (11), 3431-3436.
15. Hodes, G., *Chemical Solution Deposition of Semiconductor Films*. M. Dekker: New-York, 2003.
16. Kayanuma, Y., Quantum-size effects of interacting electrons and holes in semiconductor microcrystals with spherical shape. *Physical Review B* **1988,** 38, (14), 9797-9805.
17. Dember, H., Über eine photoelektronische Kraft in Kupferoxydul-Kristallen (Photoelectric E.M.F. in Cuprous-Oxide Crystals). *Z. Phys.* **1931,** 32, 554
18. Neo, D. C. J.; Cheng, C.; Stranks, S. D.; Fairclough, S. M.; Kim, J. S.; Kirkland, A. I.; Smith, J. M.; Snaith, H. J.; Assender, H. E.; Watt, A. A. R., Influence of Shell Thickness and Surface Passivation on PbS/CdS

Core/Shell Colloidal Quantum Dot Solar Cells. *Chemistry of Materials* **2014**, 140617071704002.

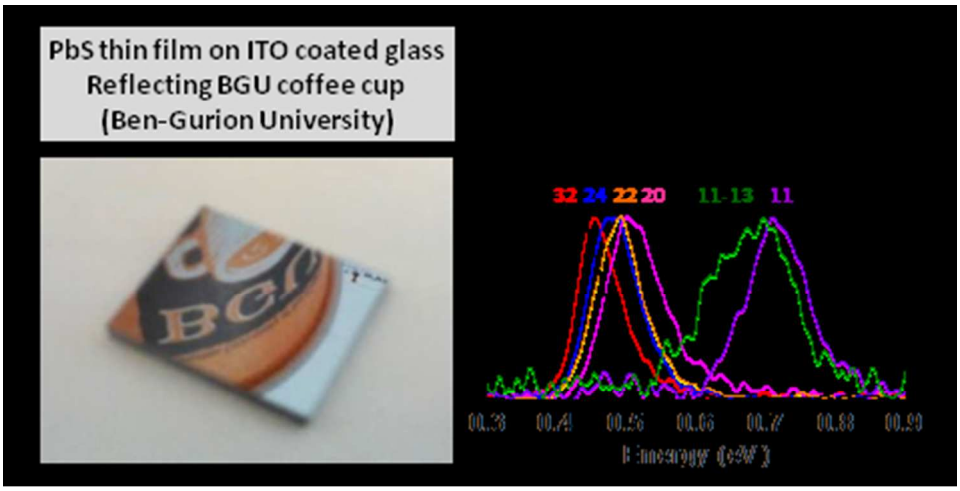

80x40mm (150 x 150 DPI)